

Computation and consequences of high order amplitude and parameter dependent tune shifts in storage rings for high precision measurements

Adrian Weisskopf*, David Tarazona, Martin Berz

*Department of Physics and Astronomy, Michigan State University, 567 Wilson Road
East Lansing, Michigan 48825, USA*

Received Day Month Year

Revised Day Month Year

Nonlinear effects of the various electric field and magnetic field components of storage rings to confine the particles and bend their trajectory can cause substantial amplitude dependent tune shifts within the beam. Furthermore, tune shifts are often sensitive to variations of system parameters, e.g. total particle momentum offsets δp . Such amplitude and parameter dependent tune shifts influence the dynamics and stability of a beam in particle storage rings. Thus, it is critical for high precision measurements to analyze and understand these influences. On this basis, we present normal form methods for the calculation of high order amplitude and system parameter dependencies of the horizontal and vertical tunes in storage rings using the differential algebra framework within COSY INFINITY. A storage ring is simulated using COSY INFINITY to generate a differential algebra Poincaré return map describing the transverse phase space behavior after each revolution in the storage ring. The map is expanded around the parameter dependent closed orbit of the system before transforming the resulting map into normal form coordinates to extract the high order tune dependencies on the phase space amplitude and variation in the system parameters. As a specific example, a storage ring similar to the Storage Ring of the Muon $g-2$ Experiment at Fermilab (E989) is investigated.

Keywords: Betatron tune shifts; high order transfer maps; nonlinear effects; normal form methods; storage ring

1. Introduction

In the limit of infinitely many revolutions in the storage ring, the horizontal and vertical tunes can be interpreted as the fractional part of the average number of horizontal and vertical phase space revolutions around the fixed phase space state of a reference particle per storage ring revolution. Tune shifts indicate how the tunes change depending on variations of the phase space amplitude relative to the reference particle and on variations in system parameters, for example, offsets in the initial momentum relative to the reference particle.

Accordingly, amplitude and parameter dependent tune shifts relative to the tune of the reference particle lead to particles within the beam that oscillate at different

*weisskop@msu.edu

frequencies, which potentially influences the beam's susceptibility to resonances.

In this paper, we present methods to calculate the horizontal and vertical tune shifts and show their behavior dependent on the phase space amplitude \vec{r}_{NF} relative to the fixed phase space state of a reference particle on the closed orbit of the respective storage ring and dependent on variations in the system parameters $\vec{\eta}$. Each storage ring is simulated using the differential algebra (DA) framework implemented within COSY INFINITY.^{1,2} From the storage ring simulation, a Poincaré return map is obtained, which describes the horizontal and vertical phase space behavior after each storage ring revolution within a Poincaré surface corresponding to the transverse cross section of the storage ring at a specific azimuth location. The Poincaré return map is expanded in the phase space coordinates \vec{z} relative to the ideal orbit of the storage ring and is also expanded in $\vec{\eta}$.

Using DA normal form methods, we analyze the phase space behavior relative to the fixed point of the Poincaré return map which corresponds to the closed orbit of the storage ring model. The normal form algorithm transforms the Poincaré return map to normal form coordinates in which the motion is rotationally invariant. Hence the phase space orbits are circular and the phase space angle advancement after each revolution in the storage ring is constant along the phase space orbit. This allows for a straightforward extraction of the tunes and tune shifts from the constant angle advancement which is given in high order dependence on the normal form phase space amplitudes \vec{r}_{NF} and on $\vec{\eta}$.

In section 4.1, we investigate specific example storage rings with our methods, namely storage rings with properties very similar to the Storage Ring of the Muon $g-2$ Experiment at Fermilab (E989).^{3,4} The results are presented and compared with preliminary measurements of the tunes and results on the decoherence rate of the muon $g-2$ beam presented in Ref. 5.

2. Differential Algebra Methods

The methods in this paper are hybrids of numerical and analytical techniques, based on a DA framework which was first developed to its current extent by Berz *et al.* (Refs. 6–8). The following summary and introduction to the DA framework, DA maps and the DA normal form algorithm are based on Ref. 6.

2.1. The Differential Algebra Framework

The basic goal of the DA framework is the representation and manipulation of analytic functions. To standardize the notation, an analytic function f is expressed up to order m in terms of its Taylor polynomial expansion \mathcal{T}_f , similar to how real numbers are approximated to a certain arbitrary number of significant digits. Instead of just using ' \approx ' to represent the approximation, the notation ' $=_m$ ' is used to indicate that both sides agree up to expansion order m . Because of the approximation, multiple functions may be represented by the same Taylor polynomial of order m and are therefore equivalent up to that order.

This gives rise to the definition of equivalence classes following Ref. 6. The equivalence class $[f]_m$ represents all elements f of the vector space of infinitely differentiable functions $\mathcal{C}^\infty(\mathbb{R}^n)$ with n real variables that have identical derivatives at the origin up to order m . The origin is chosen out of convenience and without loss of generality, any other point may be selected. In the DA framework, the equivalence class $[f]_m$ is represented by a DA vector which stores all the coefficients of the Taylor expansion of f and corresponding orders of the variables in an orderly fashion. Operations are now defined on the vector space ${}_mD_n$ of all the equivalence classes $[]_m$.

There are three operations: vector addition, vector multiplication, and scalar multiplication, which are equivalent to the truncated result of adding two polynomials, multiplying two polynomials and multiplying a polynomial with a scalar, respectively. The first two operations on the equivalence classes represented by DA vectors turn it into a ring. The scalar multiplication makes the three operations on the real or complex DA vectors an algebra, where not every element has a multiplicative inverse. An intuitive example of such elements with no inverse are functions expanded at zero without a constant part. To make the algebra a differential algebra, the derivation ∂ satisfying Leibniz's law $\partial(fg) = f\partial(g) + g\partial(f)$ is introduced (see Ref. 6 for details), which is almost trivial in the context of differentiating polynomial expansions. The derivation allows the algebraic treatment of ordinary and partial differential equations as it is common in the study of differential algebras.⁹⁻¹¹

Implemented in COSY INFINITY,^{1,2} the DA framework allows preserving the algebraic structure up to arbitrary order while manipulating the coefficients of the DA vectors with floating point accuracy. An example of DA vectors in the application of DA transfer maps and Poincaré maps is given below.

2.2. DA Transfer Maps and Poincaré Maps

Transfer maps are a standard tool in dynamical systems theory to represent the effect of the flow generated by a set of ordinary differential equations (ODE). They are also called flows, propagators, or simply maps. Basically, a transfer map \mathcal{M} algebraically expresses how a final state \vec{z}_f depends on an initial state \vec{z}_i and the system parameters $\vec{\eta}$,

$$\vec{z}_f = \mathcal{M}(\vec{z}_i, \vec{\eta}). \quad (1)$$

In the DA framework, a map is represented by a local expansion of \mathcal{M} in $(\vec{z}, \vec{\eta})$ up to order m around an expansion point \vec{z}_0 and a reference set of parameters $\vec{\eta}_0$.

There are special transfer maps, called Poincaré maps,¹² that constrain the initial and final state to Poincaré surfaces \mathbb{S}_i and \mathbb{S}_f , respectively. For the simulation of storage rings and their particle optical elements, this concept is used to represent how the state directly after an element depends on system parameters and the state directly before the element. A set-up of multiple consecutive storage ring elements is described by the composition of their Poincaré maps.

Poincaré return maps represent the case where \mathbb{S}_i is equal to \mathbb{S}_f . Poincaré return maps are particularly useful for repetitive systems like the one considered in this paper, where multiple applications of the Poincaré return map correspond to a propagation of the system, for example, multiple storage ring revolutions. For these applications, it is advantageous if the map is origin preserving, i.e. the expansion point is a fixed point of the map, because system dynamics represented by origin preserving Poincaré return maps can be further analyzed by normal form methods and for the asymptotic stability of the system.

Constraining the map to the Poincaré surface \mathbb{S} is often done by calculating the flow of an ODE and projecting the flow onto the surface \mathbb{S} to generate the Poincaré map. An implementation of a timewise projection onto a surface \mathbb{S} defined by $\sigma(\vec{z}, \vec{\eta}) = 0$ is outlined in Ref. 13.

2.3. DA Normal Form Algorithm

For an origin preserving Poincaré return map \mathcal{M} of a repetitive Hamiltonian system dependent on phase space coordinates $\vec{z} = (\vec{q}, \vec{p})$, the DA normal form algorithm⁶ performs a nonlinear change of variables to rotationally invariant normal form coordinates $(\vec{q}_{\text{NF}}, \vec{p}_{\text{NF}})$ by an order-by-order transformation. For parameter $\vec{\eta}$ dependent systems, the first step of the algorithm is determining the parameter dependent fixed point of the map and expanding the map around it. This will be further discussed with regard to closed orbits of the specific system in section 3.2.

In the first order transformation, the map is diagonalized. For this we require that the map is linearly stable, i.e. eigenvalues λ_i with $|\lambda_i| \leq 1$, and that the eigenvalues are distinct. Most relevant and particularly important for the application in this paper are symplectic maps, for which the eigenvalues come in complex conjugate pairs $\lambda_k^\pm = \exp(\pm i\mu_k)$ of magnitude 1. The corresponding diagonalization transforms the system into the basis of the complex conjugate eigenvector pairs of its linear part.

The nonlinear transformations \mathcal{A}_m are determined one order after another starting with order $m = 2$. The transformations are given by $\mathcal{A}_m = {}_m\mathcal{I} + \mathcal{T}_m$, where \mathcal{T}_m consists of polynomials of order m only and \mathcal{I} is the identity of the current variables. The goal is finding \mathcal{T}_m such that the m th order of the map \mathcal{M}_{m-1} is simplified or even eliminated when the transformation \mathcal{A}_m and its inverse $\mathcal{A}_m^{-1} = {}_m\mathcal{I} - \mathcal{T}_m$ are applied to it. The following equations illustrate how \mathcal{T}_m is determined for the m th order.

Given the map \mathcal{M}_{m-1} , representing \mathcal{M} simplified up to order $m-1$, and applying \mathcal{A}_m and its inverse to it, as shown in Eq. 7.60 in Ref. 6, yields

$$\begin{aligned} \mathcal{A}_m \circ \mathcal{M}_{m-1} \circ \mathcal{A}_m^{-1} &= {}_m(\mathcal{I} + \mathcal{T}_m) \circ (\mathcal{R} + \mathcal{S}_{<m}^* + \mathcal{S}_m) \circ (\mathcal{I} - \mathcal{T}_m) \\ &= {}_m(\mathcal{I} + \mathcal{T}_m) \circ (\mathcal{R} - \mathcal{R} \circ \mathcal{T}_m + \mathcal{S}_{<m}^* + \mathcal{S}_m) \\ &= {}_m\mathcal{R} + \mathcal{S}_{<m}^* + \mathcal{S}_m + [\mathcal{T}_m, \mathcal{R}], \end{aligned} \quad (2)$$

where \mathcal{R} is the diagonalized linear part and $\mathcal{S}_{<m}^*$ are the simplified terms of previous

transformations of order $< m$. $[\mathcal{T}_m, \mathcal{R}]$ denotes the commutator of \mathcal{T}_m and \mathcal{R} and \mathcal{S}_m represents only the m th order terms of the map \mathcal{M}_{m-1} , namely the leading order of terms that are not simplified yet. In the equations above, only terms up to order m are considered, since terms of order $m+1$ and larger are irrelevant for determining \mathcal{T}_m . Nonetheless, the influence of the m th order transformation on the higher orders of the map is non-trivial and can affect higher order transformations and the resulting normal form significantly.

The maximum simplification of the order m terms of \mathcal{M}_{m-1} , namely \mathcal{S}_m , would be achieved by finding \mathcal{T}_m such that the commutator $\mathcal{C}_m = \mathcal{T}_m \circ \mathcal{R} - \mathcal{R} \circ \mathcal{T}_m = [\mathcal{T}_m, \mathcal{R}]$ and \mathcal{S}_m cancel each other, which would eliminate all nonlinear terms of order m . The following calculation illustrates why this is not always possible.

In the j th subspace, the coefficients of the terms $\prod_i q_i^{k_i^+} p_i^{k_i^-}$ of \mathcal{C}_m are denoted with $(\mathcal{C}_{m,j}^+ | \vec{k}^+, \vec{k}^-)$ for the position component of the subspace, and $(\mathcal{C}_{m,j}^- | \vec{k}^+, \vec{k}^-)$ for the complex conjugate momentum component of the subspace. In particular, the commutator coefficient

$$\left(\mathcal{C}_{m,j}^\pm | \vec{k}^+, \vec{k}^- \right) = \left(\mathcal{T}_{m,j}^\pm | \vec{k}^+, \vec{k}^- \right) \cdot \left(e^{i\vec{\mu} \cdot (\vec{k}^+ - \vec{k}^-)} - e^{\pm i\mu_j} \right) \quad (3)$$

is zero for $\text{mod}_{2\pi}(\vec{\mu} \cdot (\vec{k}^+ - \vec{k}^-) \mp \mu_j) = 0$. This condition is satisfied for terms with $a_j - b_j = \pm 1$ and $a_i = b_i \forall i \neq j$. Accordingly, the corresponding nonlinear terms $(\mathcal{S}_{m,j}^\pm | \vec{k}^+, \vec{k}^-)$ cannot be canceled and hence survive. These surviving terms \mathcal{S}_m^* of \mathcal{S}_m describe the entire dynamics of the systems in a nutshell and are the key elements of the further dynamic analysis. All the other nonlinear terms $(\mathcal{S}_{m,j}^\pm | \vec{k}^+, \vec{k}^-)$ are canceled by choosing

$$\left(\mathcal{T}_{m,j}^\pm | \vec{k}^+, \vec{k}^- \right) = \frac{-\left(\mathcal{S}_{m,j}^\pm | \vec{k}^+, \vec{k}^- \right)}{e^{i\vec{\mu} \cdot (\vec{k}^+ - \vec{k}^-)} - e^{\pm i\mu_j}}. \quad (4)$$

Note that the surviving terms of higher order transformations can be influenced significantly by the previous transformations and hence their coefficients of \mathcal{T}_m . Eq. 4 indicates that a coefficient of \mathcal{T}_m is large, if the denominator is close to zero i.e. satisfying the resonance condition, and/or the corresponding coefficient of \mathcal{S}_m in the numerator is large.

After the nonlinear transformations, the map is transformed back into real space by using the real and imaginary components of each of the current complex conjugate eigenvector pairs as new basis. As a result of the order-by-order transformation and the transformation to real space, the original map is significantly simplified up to an arbitrary order to a rotationally invariant normal form map \mathcal{M}_{NF} with only amplitude \vec{r}_{NF} and parameter $\vec{\eta}$ dependent angle advancements $\Lambda(\vec{r}_{\text{NF}}, \vec{\eta})$ in the normal form phase space (see one-dimensional example in Fig. 1).

In the j th subspace, the map in normal form coordinates is given by

$$\mathcal{M}_{\text{NF},j} = \begin{pmatrix} \cos(\Lambda(\vec{r}_{\text{NF}}, \vec{\eta})) - \sin(\Lambda(\vec{r}_{\text{NF}}, \vec{\eta})) \\ \sin(\Lambda(\vec{r}_{\text{NF}}, \vec{\eta})) \cos(\Lambda(\vec{r}_{\text{NF}}, \vec{\eta})) \end{pmatrix} \cdot \begin{pmatrix} q_{\text{NF},j} \\ p_{\text{NF},j} \end{pmatrix}. \quad (5)$$

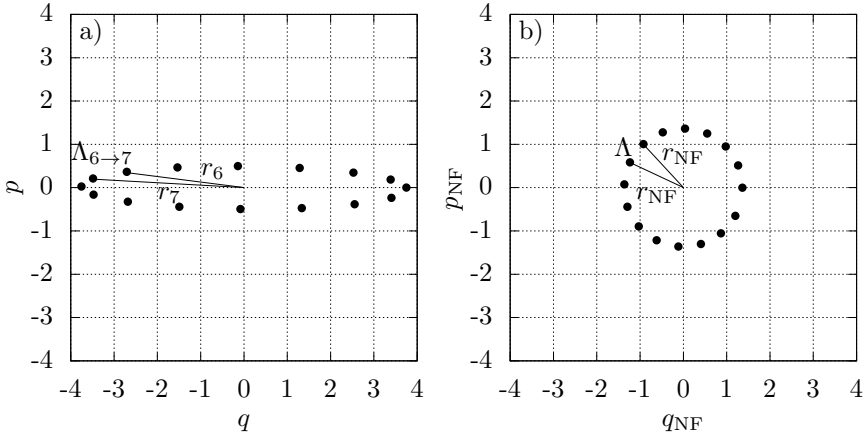


Fig. 1. In a), the phase space state (q_0, p_0) is iterated 16 times with the Poincaré return map. The phase space angle advancement $\Lambda_{k \rightarrow k+1}$ and the phase space radii r_k change along each of the phase space orbits. In b), the corresponding normal form state $(q_{\text{NF}}, p_{\text{NF}})$ is iterated 16 times with the corresponding normal form map. The normal form phase space behavior is rotationally invariant with a constant normal form radius r_{NF} for each of the phase space orbits, and a constant but amplitude and parameter dependent angle advancement $\Lambda(r_{\text{NF}}, \vec{\eta})$ for each of the phase space orbits.

The rotational invariance implies an interpretation of the normal form as an averaged representation of the Poincaré return map in the limit where the map application is repeated infinitely many times. In one dimension, the normal form radius corresponds the invariant amplitude of the original phase space motion. For systems with more dimensions, the association of the original phase space subspaces with normal form subspaces and its angle advancement and invariant normal form radius is only appropriate if there is no or only very weak linear coupling between the original phase space subspaces, since the normal form space corresponds to the decoupled phase space from the diagonalization.

The normal form transformation $\mathcal{A}(\vec{q}, \vec{p}, \vec{\eta})$ provides the connection between the original coordinates and the normal form coordinates and is the result of the composition of all the involved transformations: the parameter dependent fixed point transformation, diagonalization, nonlinear transformations and the transformation back to real space.

3. From storage ring models to tune dependencies

3.1. Storage ring simulation using Poincaré maps

A storage ring is composed of various particle optical elements, each of which can be simulated in COSY INFINITY,^{1,2} mostly by a multipole expansion of the involved fields or corresponding potentials.

For each particle optical element, there is a hypothetical ideal orbit for which it is calibrated, usually along the center of the element. The ideal orbit is characterized

by a predetermined set of system parameters $\vec{\eta}_0$, for example a specific total reference momentum of the particles. If the element is simulated as ideal, namely without perturbations, the actual trajectory of a particle initiated on the ideal orbit when entering the element (at \vec{z}_0) follows the ideal orbit throughout the element. However, with perturbations like imperfections in the associated fields of the element, a particle initiated at \vec{z}_0 might follow a trajectory different from the ideal orbit. Hence the ideal orbit describes the actual trajectory of a particle initiated at \vec{z}_0 in the unperturbed case.

To analyze how an element influences the transverse phase space behavior around the ideal orbit, Poincaré maps are used. The Poincaré surfaces correspond to the vertical storage ring cross section before (\mathbb{S}_i) and after the element (\mathbb{S}_f). The Poincaré map \mathcal{P} is expanded around the ideal orbit and expresses how the relative phase space state $\vec{z}_f \in \mathbb{S}_f$ after the particle optical element depends on variations in $\vec{\eta}$ and on the relative phase space state $\vec{z}_i \in \mathbb{S}_i$ before the element, with $\vec{z}_f = \mathcal{P}(\vec{z}_i, \vec{\eta})$. The phase space states relative to the ideal orbit \vec{z} consist of the horizontal $(q_1, p_1) = (x, a)$ and vertical $(q_2, p_2) = (y, b)$ phase space components within the Poincaré surface \mathbb{S} . For unperturbed elements, the Poincaré map \mathcal{P} is origin preserving, with $\mathcal{P}(\vec{0}, \vec{0}) = \vec{0}$, since the trajectory follows the ideal orbit - the expansion point of the map.

The transverse phase space behavior after a full revolution in the storage ring is given by the Poincaré return map \mathcal{M} , which is generated by composing the individual Poincaré maps \mathcal{P}_i of the individual storage ring elements according to the storage ring set-up ($\mathcal{M} = \mathcal{P}_k \circ \mathcal{P}_{k-1} \circ \dots \circ \mathcal{P}_2 \circ \mathcal{P}_1$) such that the composed ideal orbit is a closed orbit.

3.2. Closed orbits under perturbation

For the use of the DA normal form algorithm, it is essential that the Poincaré return map is origin preserving, hence a fixed point map where the expansion point belongs to a closed orbit that returns to itself after each storage ring revolution. If all components are simulated to be unperturbed, then the Poincaré return map is a composition of origin preserving Poincaré maps and hence also origin preserving. However, if the simulation considers perturbations, the actual trajectory of the expansion point may be distorted from the ideal orbit and hence not a closed orbit. Hence the expansion point of the associated Poincaré return map may not be a fixed point and the map may not be origin preserving.

However, if the perturbation is sufficiently small, then a fixed point \vec{z}_{FP} will continue to exist, as we will show now. Parameterizing the strength of the perturbation with $\vec{\eta}$, the origin preserving fixed point map of the unperturbed system is given by $\mathcal{M}(\vec{z}, \vec{\eta} = 0)$. To analyze the preservation of the parameter dependent fixed point, an extended map $\mathcal{N}(\vec{z}, \vec{\eta}) = (\mathcal{M}(\vec{z}, \vec{\eta}) - \vec{z}, \vec{\eta})$ is defined. If $\det(\text{Jac}(\mathcal{N}(\vec{z}, \vec{\eta})))|_{(\vec{z}, \vec{\eta})=(\vec{0}, \vec{0})} \neq 0$ then, according to the inverse function theorem, an inverse of the map \mathcal{N} exists for a neighborhood \mathbb{D} around the evaluation point $(\vec{0}, \vec{0})$ of the Jacobian.

The parameter dependent fixed point $\vec{z}_{\text{FP}}(\vec{\eta})$ of \mathcal{M} and hence the closed orbit of the system exists as long as $(0, \vec{\eta})$ is within the neighborhood for which invertibility has been asserted. If this is the case and the inverse \mathcal{N}^{-1} around $(\vec{0}, \vec{0})$ is given, then the parameter dependent fixed point can be calculated via

$$(\vec{z}_{\text{FP}}(\vec{\eta}), \vec{\eta}) = \mathcal{N}^{-1}(\vec{0}, \vec{\eta}). \quad (6)$$

Re-expanding the map around the parameter dependent fixed point yields the origin preserving Poincaré return map under perturbations in the system parameters.

3.3. *Tunes, tune shifts, normal form radii and resonances*

DA normal form methods are used to transform the origin preserving phase space Poincaré return map to the rotationally invariant normal form as shown in Eq. 5. From the normal form, the angle advancement $\Lambda(\vec{r}_{\text{NF}}, \vec{\eta})$ as a function of amplitude \vec{r}_{NF} and system parameter $\vec{\eta}$ is particularly straightforward to extract. Scaling the angle advancement to 1 instead of 2π provides the number of phase space revolutions per system revolution, represented by the Poincaré return map. In beam physics terminology, the parameter independent frequency of normal form phase space revolutions is known as the tune ν , whereas the frequencies change dependent on \vec{r}_{NF} and $\vec{\eta}$ are called the amplitude and parameter dependent tune shifts $\delta\nu(r_{\text{NF},k}, \vec{\eta})$, respectively.

The tune ν_k corresponds to the scaled phase μ_k of the complex conjugate eigenvalues λ_k^\pm of the linear transformation. Hence the tune is related to the linear motion around the expansion point - the motion ‘infinitely near’ the expansion point. Interpreting the tune and its tune shifts as the phase space rotation frequency suggests that the tune - the phase space rotation frequency of the expansion point - is a rotation with no amplitude, where the frequency is determined by the linear motion around the expansion point. In particular, this means that maps with the same expansion point can have different tunes depending on the linear motion around it. For parameter dependent systems, the tunes of the parameter dependent closed orbit can already be determined by $\vec{\nu}(\vec{\eta}) = \vec{\mu}(\vec{\eta})/2\pi$ in the parameter dependent linear transformation.

The tune shifts indicate the change of the phase space rotation frequency dependent on the phase space amplitudes \vec{r}_{NF} and variations in the system parameters $\vec{\eta}$. Since the normal form transformation is symplectic, it preserves the phase space volume, which helps to understand the connection between the original coordinates and their normal form radii. Given sufficiently linearly decoupled phase space subspaces, the normal form radius $r_{\text{NF},k}$ is a measure for the invariant phase space area of the k th subspace. Hence the original coordinates of an invariant phase space orbit in the k th subspace enclosing the area A_k correspond to the normal form radius $r_{\text{NF},k} = \sqrt{A_k/\pi}$.

The normal form radii are the link between the tune dependencies and the original coordinates. The dependency of the tune shifts on the normal form radii is

a result of the surviving terms \mathcal{S}_m of the nonlinear normal form transformations. But the crucial terms are the \mathcal{T}_m from Eq. 4 that are used to cancel all the other nonlinear terms \mathcal{S}_m . On the one hand, the \mathcal{T}_m terms determine how the original coordinates $\vec{z} = (\vec{q}, \vec{p})$ and the system parameters $\vec{\eta}$ relate to the normal form radii \vec{r}_{NF} , since the \mathcal{T}_m are the essential part of the normal form transformation. On the other hand, they influence the higher order nonlinear terms \mathcal{S}_l with $l > k$, which either survive and determine the dependency of the tune shifts on the normal form radii, or they determine the higher order terms \mathcal{T}_l .

The denominator of \mathcal{T}_m in Eq. 4 has a potentially large effect on its size the closer it is to satisfying the resonance condition

$$\text{mod}_{2\pi}((k_1^+ - k_1^-) \cdot \mu_x + (k_2^+ - k_2^-) \cdot \mu_y \mp \mu_i) = \text{mod}_1(u \cdot \nu_x + w \cdot \nu_y) = 0, \quad (7)$$

where the order of the transformation $m = k_\eta + \sum_i (k_i^+ + k_i^-)$ relates to the order of the resonance $n = |u| + |w|$ with $m = n \pm 1$ and $k_i^+, k_i^-, k_\eta, u, w \in \mathbb{Z}$. k_η denotes the order of the parameter dependence. So if the tunes $\vec{\nu}$ are close to satisfying a resonance condition of order n , the nonlinear transformations of order $m = n \pm 1$ have potentially large terms \mathcal{T}_m , which determine the relation of original coordinates to normal form coordinates and influence the higher order, potentially surviving terms of the map and hence the tune shifts. Resonances of order $n = |u| + |w|$ are denoted with $n(u, w)$.

4. Storage ring simulation and example results

In the following we present an illustrative example for the methods derived above. We choose a small ring that is to be expected to show a large amount of amplitude dependent tune shifts due to the presence of strong high order nonlinearities. The purpose of the ring is to store muons and analyze their magnetic moment, and the presence of the nonlinearities affects the ability to store particles without losses.

4.1. Storage ring simulation

For the simulation of the muon $g-2$ storage ring, a detailed nonlinear model¹⁴ of the storage ring has been set up using COSY INFINITY. The simulation considers the magnetic field that guides the beam around the storage ring and the four-fold symmetric electrostatic quadrupole system¹⁵ (EQS), which focuses the beam vertically. Additionally, perturbations due to the EQS fringe fields and imperfections in the vertical magnetic field are taken into account.

The model¹⁴ represents the magnetic field inhomogeneities by fitting 2D magnetic multipoles up to fifth order to measurement data of the magnetic field within the muon $g-2$ storage ring (see Ref. 14 for details). The EQS is considered by the corresponding electrostatic potential as a 2D multipole expansion up to tenth order to accurately model the nonlinearities of the system up to the significant contribution of the 20th-pole. The fringe fields of the EQS - the fall-off of the electric field at

the edges of the EQS components - are simulated based on numerical calculations performed with the code COULOMB.¹⁶

From the earlier mentioned cases, Poincaré return maps of order ten of the muon $g-2$ storage ring are obtained following section 3.1 and expanded in the horizontal (x, a) and vertical (y, b) phase space coordinates relative to the ideal orbit of the respective storage ring simulation. Additionally, the maps are expanded in relative offset $p = \Delta p/p_0$ with respect to the initial reference momentum p_0 to represent particles within the momentum acceptance range of $\pm 0.5\%$ of the E989 storage ring. The relative change δp corresponds to the change of the system parameter $\vec{\eta}$.

To distinguish the influences of various elements of the storage ring and their perturbations, it is useful to simulate different configurations of the components. For the muon $g-2$ storage ring, we simulate the following three storage ring configurations to analyze the influence of perturbations due to EQS fringe fields and imperfections in the vertical magnetic field:

- E_0B_0 : No EQS fringe fields and a perfect magnetic field
- E_fB_0 : With EQS fringe fields and a perfect magnetic field
- E_0B_i : No EQS fringe fields and an imperfect magnetic field

The Poincaré return map of a storage ring considering both the EQS fringe fields and the imperfections of the magnetic field simultaneously, E_fB_i in the nomenclature from above, is still under investigation, since superimposing two perturbations is problematic for technical reasons. Hence the E_fB_i case is not considered here.

Additionally, each of the configurations is considered at two different EQS voltage V_{EQS} , namely at 18.3 kV and 20.4 kV. These specific voltages were chosen to recreate similar employed operating points during initial runs of E989.

The calculated Poincaré return maps expanded around the ideal orbit of the muon $g-2$ storage ring show strong ninth order nonlinearities, which are associated to the significant field contributions of the 20th order multipole of the EQS potential. The relevance of these dominant ninth order nonlinear terms will be discussed throughout the next subsections.

4.2. Closed orbits of storage ring models

The ideal orbit of the E989 storage ring is the closed orbit of the unperturbed case E_0B_0 . It lies within the horizontal plane along the center of the storage ring.

Due to the symmetry of the EQS with respect to the horizontal plane and its calibration for the ideal orbit, under perfect conditions, its influences cancel out perfectly along the ideal orbit. Accordingly, the Poincaré return map expansion of E_0B_0 around the ideal orbit it is an origin preserving fixed point map.

Considering the fringe fields for E_fB_0 as a perturbation to the E_0B_0 case slightly breaks the symmetry of the EQS, but since this influence is negligibly small along the ideal orbit, it can also be considered the closed orbit of the E_fB_0 case. Hence for all four cases of the muon $g-2$ storage ring model with a perfectly vertical magnetic

field, the ideal orbit is a closed orbit of the respective system.

However, the cases with imperfections in the magnetic field (E_0B_i) introduce uneven vertical and radial forces along the ideal orbit and break the symmetry with respect to the horizontal plane. Thus, expanding the Poincaré map \mathcal{M} around the ideal orbit (fixed point of the magnetically unperturbed system) does not yield a origin preserving fixed point map. Since the conditions for the preservation of the fixed point is satisfied under this perturbation, the maps of the E_0B_i cases are re-expanded around their respective fixed points \vec{z}_{FP} relative to the ideal orbit along the center of the simulated example muon $g-2$ storage ring:

$$\begin{aligned}\vec{z}_{\text{FP}} &= (-0.65 \text{ mm}, -0.13 \text{ mrad}, 2.24 \text{ mm}, 0.07 \text{ mrad}) \text{ for } 18.3 \text{ kV and} \\ \vec{z}_{\text{FP}} &= (-0.58 \text{ mm}, -0.11 \text{ mrad}, 1.99 \text{ mm}, 0.07 \text{ mrad}) \text{ for } 20.4 \text{ kV.}\end{aligned}\quad (8)$$

4.3. Momentum dependence of closed orbit

Following Eq. 6, the parameter dependent fixed point of the origin preserving Poincaré return maps are calculated, which correspond to the dependence of the respective closed orbits on offsets δp from the reference momentum p_0 . Fig. 2 illustrates how each of the phase space components of the respective closed orbits depends on δp at the specific azimuth location of the Poincare surface in the storage ring.

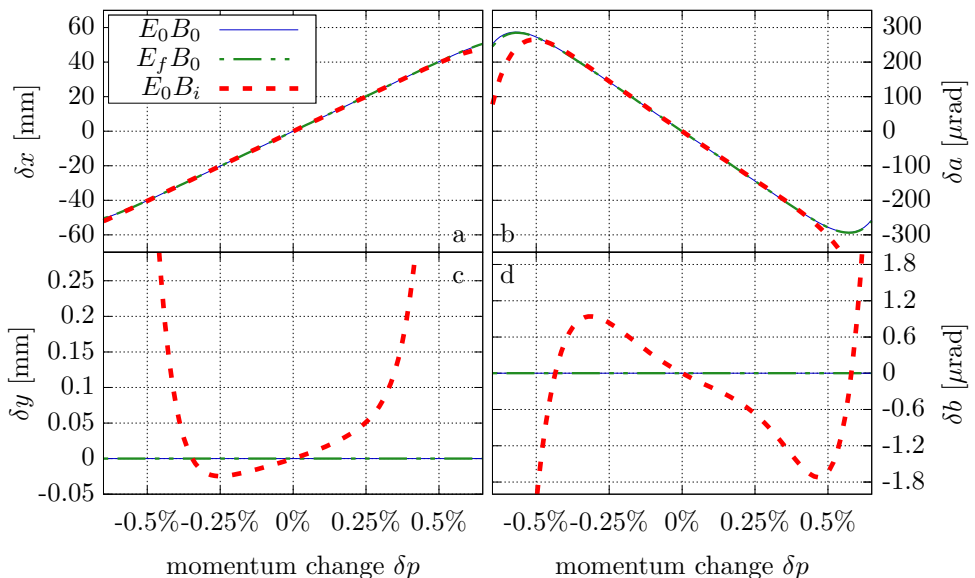


Fig. 2. Changes of the closed orbits due to relative changes δp in the total initial momentum. Changes to the horizontal components of the respective closed orbit are shown in the upper plots: a) x and b) a . Changes to the vertical components, which only occur in the E_0B_i case, are shown in the lower plots: c) y and d) b . The plots only illustrate changes and no absolute position of the closed orbits. The influence of the EQS and its fringe fields on the closed orbit are minimal such that the plots represent both cases at 18.3 kV and 20.4 kV EQS voltage.

The primary effect of the momentum change, namely, the change of the orbit radius, is clearly visible in the illustration of the horizontal components for all three cases. The associated dependence of the horizontal momentum is caused by the changing orientation of the momentum dependent closed orbit with respect to the Poincare surface. The illustration also shows that the secondary effects from the nonlinearities of the EQS, its fringe fields and the imperfections in the magnetic field are weak in comparison over the momentum acceptance range of $\pm 0.5\%$.

Due to the symmetry of the EQS with respect to the horizontal plane, the vertical components of the EQS and its fringe fields cancel out within the horizontal plane and hence do not by themselves introduce vertical motion for the momentum dependent. Hence the closed orbit of the cases with a perfectly vertical magnetic field (E_0B_0 and E_fB_0) stay within the horizontal plane for relative offsets δp from the reference momentum p_0 .

Since the magnetic field imperfections already force the closed orbit of the E_0B_i case out of the horizontal plane and the combined nonlinear effects distort it from its original circular shape, a relative offset from the reference momentum causes primary effects in the horizontal components and secondary effects in both the horizontal and vertical components. In particular, it shows that the secondary effects of the E_0B_i case in the vertical components are about three orders of magnitude weaker than the primary effect in the horizontal components.

The results for the two EQS voltages over the illustrated range are very similar (hence not displayed) but not identical, which further indicates the magnitude of the secondary effects due to the EQS and changes to its voltage compared to the primary radius change.

The primary effect in the horizontal fixed point component is linearly dominated over the momentum acceptance range of $\pm 0.5\%$, with about 80 mm/% for x and about -0.53 mrad/% for a . For the E_0B_i case, the secondary effects in the vertical components can be linearly approximated over a momentum spread of $\pm 0.25\%$, where y changes with about 130 $\mu\text{m}/\%$ and b changes with about -2.6 $\mu\text{rad}/\%$.

4.4. Tunes and their parameter dependence

Given the parameter dependent fixed point map representing the phase space behavior around the momentum dependent closed orbit of the muon $g-2$ storage ring model, the diagonalization in the DA normal form algorithm is used to determine the tunes of the closed orbits and their momentum δp dependence. Table 1 shows the values of the tunes and their linear dependencies on δp , which are called chromaticities and denoted with ξ_i . Fig. 3 illustrates the full dependencies of the tunes on relative offsets δp from the reference momentum p_0 .

The tunes in Table 1 indicate a strong influence of the EQS voltage on the linear motion around the respective expansion points. Hence an appropriate EQS voltage is critical to ensure tunes far away from resonance conditions as given in Eq. 7.

The perturbations in the storage ring configuration, namely the EQS fringe

Table 1. Horizontal and vertical tunes ν_i and their chromaticities (linear momentum dependence) ξ_i for the simulation of the muon $g-2$ storage ring of E989 at EQS voltages of 18.3 kV and 20.4 kV.

Case	ν_x	ν_y	ξ_x	ξ_y
E_0B_0 (18.3 kV)	0.94445665	0.33082727	-0.13144836	0.39090599
E_fB_0 (18.3 kV)	0.94446284	0.33080860	-0.13145198	0.39093897
E_0B_i (18.3 kV)	0.94456336	0.33051804	-0.15174178	0.44714448
E_0B_0 (20.4 kV)	0.93792503	0.34941528	-0.14993480	0.42115341
E_fB_0 (20.4 kV)	0.93793195	0.34939552	-0.14993843	0.42118673
E_0B_i (20.4 kV)	0.93803328	0.34911988	-0.17052048	0.47444158

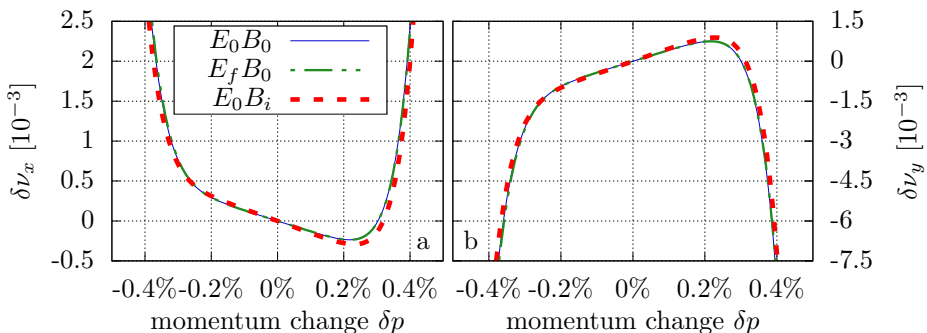


Fig. 3. Vertical and horizontal tune dependence in the model of the muon $g-2$ storage ring of E989 on relative offsets δp from the reference momentum p_0 . The plots represent both EQS voltages since the differences are smaller than visible in this illustration. Note that only changes relative to the tunes from Table 1 are shown.

fields (E_fB_0) and the imperfections in the magnetic field (E_0B_i), change the tunes and chromaticities relative to the unperturbed E_0B_0 case by different magnitudes. The shifts due to the magnetic field imperfections is about one order of magnitude stronger for the tunes, and three to four orders of magnitude stronger for the chromaticities than the influence of the EQS fringe fields. Both perturbations shift the tunes to larger values for ν_x and smaller values for ν_y .

While the tunes and chromaticities are majorly influenced by the perturbations in the magnetic and electric field, and especially the EQS voltage, the tune shifts behave very similarly for all three cases and for both EQS voltages.

All momentum dependent tune shifts in Fig. 3 show predominantly linear behavior for $|\delta p| < 0.25\%$, which makes the values for the chromaticities in Table 1 particularly useful. For $|\delta p| > 0.33\%$, the momentum dependent tune shifts are dominated by an order eight dependence on relative momentum offsets δp . This eighth order dependence results from the strong ninth order terms in the original map, which are linear in the phase space components and of order eight in the momentum dependence, representing the earlier mentioned significant influence of the 20th-pole of the EQS potential. For large momentum offsets of $|\delta p| > 0.33\%$, the tune shifts are positive for the horizontal component and negative for the vertical component.

4.5. Amplitude dependent tune shifts

The DA normal form algorithm provides the amplitude and parameter dependent tune shifts $\delta\nu_i(r_{\text{NF},1}, r_{\text{NF},2}, \delta p)$, where the amplitudes are given by the normal form radii $r_{\text{NF},i}$ - the invariants up to the calculation order. In this section of the analysis, we are considering only the amplitude dependence ($\delta p = 0$) of the tune shifts for each of the normal form radii separately: $\delta\nu_i(r_{\text{NF},1}, r_{\text{NF},2}=0, \delta p=0)$ and $\delta\nu_i(r_{\text{NF},1}=0, r_{\text{NF},2}, \delta p=0)$.

The normal form transformation $\mathcal{A}(\vec{z}, \delta p)$ provides the relation between the normal form radii \vec{r}_{NF} and the original coordinates \vec{z} dependent on the system parameter δp . Table 2 shows how the normal form radii depend on the individual original coordinates in regions where the dependence is linear. The constant of proportionality $\kappa_{z_i,j}$ yields $r_{\text{NF},j}(z_i, z_{l \neq i} = 0, \delta p = 0) = \kappa_{z_i,j} \cdot |z_i|$. The linear approximation of the normal form radii is given for ($|x|, |a|, |y|, |b| \leq (5 \text{ cm}, 6 \text{ mrad}, 4 \text{ cm}, 2 \text{ mrad})$). Note that the region of linear dependence between the original coordinates and normal form radii might larger than the given region for certain cases and variables.

Table 2. Linear dependence of the normal form radii $r_{\text{NF},i}$ on individual original coordinates for ($|x|, |a|, |y|, |b| \leq (5 \text{ cm}, 6 \text{ mrad}, 4 \text{ cm}, 2 \text{ mrad})$). Note that $r_{\text{NF},2}$ is about three times more sensitive to b than $r_{\text{NF},1}$ is to a , while the each of the position components have about the same influence on the respective normal form radii.

EQS voltages	$\kappa_{ x[\text{cm}] ,1}$	$\kappa_{ a[\text{mrad}] ,1}$	$\kappa_{ y[\text{cm}] ,2}$	$\kappa_{ b[\text{mrad}] ,2}$
18.3 kV	0.222	0.167	0.243	0.519
20.4 kV	0.221	0.168	0.250	0.505

Due to the symplecticity of the normal form transformation and the associated conservation of phase space volume, the linear relation between the normal form radii and the original coordinates for the given range provides the invariant phase space ellipses in the subspace of the original coordinates with

$$q_i^2 \kappa_{q_i,i}^2 + p_i^2 \kappa_{p_i,i}^2 = r_{\text{NF},i}^2 (q_i, p_i, q_{j \neq i} = 0, p_{j \neq i} = 0, \delta p = 0). \quad (9)$$

Accordingly, Table 2 and Eq. 9 help relate the following results dependent on normal form radii to amplitudes in the original coordinates.

The amplitude dependent tune shifts of the simulated cases are illustrated in Fig. 4. The amplitude dependence is never linear but always appears as even orders. Just like for the momentum dependent tune shifts, the amplitude dependent tune shifts are only weakly influenced by the EQS voltages and the field perturbations. Additionally, the amplitude dependent tune shifts are also positive for $\delta\nu_x$ and negative for $\delta\nu_y$. Furthermore, there is also the dominating eighth order dependence for $r_{\text{NF},i} \geq 0.5$, related to the strong ninth order nonlinear terms resulting from the 20th-pole of the EQS potential.

In Fig. 4 in Ref. 5, the decoherence rate Γ determined by preliminary tracking measurements and simulations of the amplitude dependent tune shifts show overall

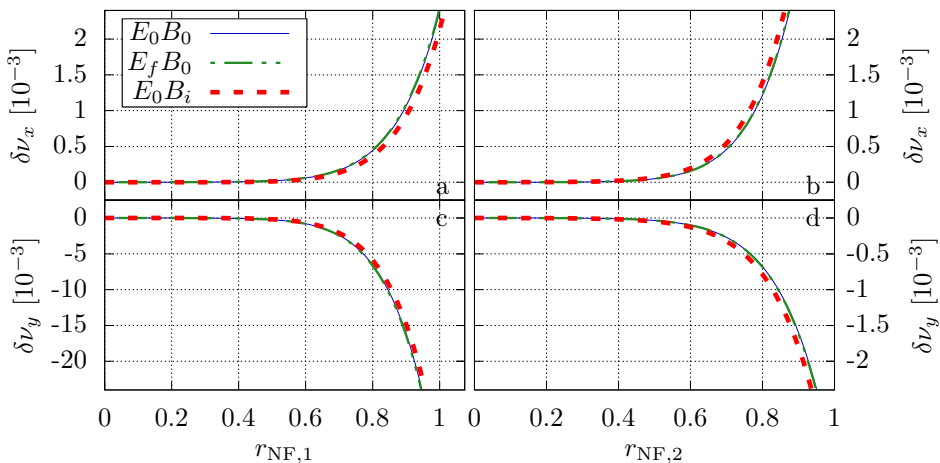


Fig. 4. Amplitude dependent tune shifts in the model of the muon $g-2$ storage ring of E989. The influence of the EQS voltage and perturbations in the fields are minimal. The amplitudes are given in terms of the normal form radii $r_{\text{NF},i}$. Note that only relative changes of the tunes in Table 1 are shown. The influence of $r_{\text{NF},2}$ on $\delta\nu_y$ is an order of magnitude smaller compared to $r_{\text{NF},1}$.

negative tune shifts when looking at the EQS influences, which are dominated by the 20th-pole of the EQS potential. These results agree with our analysis shown in Fig. 4 considering that the negative dependence of the vertical tune shifts on the normal form radius of the horizontal subspace $r_{\text{NF},1}$ are about an order of magnitude larger compared to the other positive and negative amplitude dependent tune shifts. Reasons for this particular sensitivity of the vertical tune shifts to phase space amplitudes in the horizontal subspace are given in Ref. 16.

4.6. Combined effects and tune footprint

In order to analyze combined effects of amplitude and momentum dependent tune shifts to the full extent in storage ring models, it is useful to evaluate the tunes for a realistic beam distribution. For the example storage rings, a model¹⁴ of the muon $g-2$ storage ring model based on COSY INFINITY is used to generate the beam distribution from orbit tracking of the muon beam until it is circulating in the storage ring, prepared for data analysis. In particular, the model considers the imperfect injection process, which attempts to align the injected beam with the ideal orbit of the storage ring as good as possible. The model also considers the mispowered EQS components to imitate the preparation mechanism during the first turns of the beam in the storage ring at E989. Ref. 14 further elaborates on the details of the tracking model and how a distribution is obtained.

The distributions of the variables $(x, a, y, b, \delta p)$ for the most realistic configuration of this paper ($E_0 B_i$) are considered at 18.3 kV and 20.4 kV EQS voltage. The distributions relative to their respective closed orbit are illustrated in Fig. 5 as projections into the (x, a) , (y, b) , (x, y) and (a, b) subspaces.

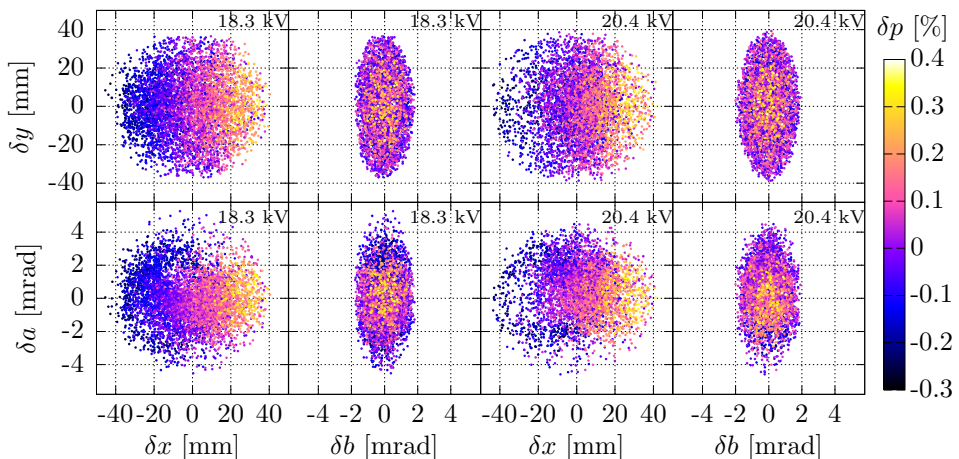


Fig. 5. Projections of the distribution of the variables $(x, a, y, b, \delta p)$ in the realistic beam simulation at 18.3 kV and 20.4 kV EQS voltage in the $E_0 B_i$ case.

In the distributions in Fig. 5, the strong positive correlation between x and δp is clearly visible, which is a result of the momentum dependence of the orbits radius: the larger δp , the larger the radius of the orbit and hence the larger x . The distributions also show a tendency to higher total momenta while overall staying well within the momentum acceptance range of $\pm 0.5\%$. The spread of the vertical momentum component b is about a factor two to three smaller than its horizontal counterpart a , while the (x, y) projection in position space shows an almost circular distribution, which agrees with the dependence of the normal form radii in Table 2.

Using DA normal form methods, the normal form transformation of the $E_0 B_i$ map at 18.3 kV and 20.4 kV EQS voltage are calculated. The dataset of all particles in the simulation $(x_i, a_i, y_i, b_i, \delta p_i)$ is used to calculate the corresponding normal form radii, $r_{\text{NF},1}$ and $r_{\text{NF},2}$, and tunes, ν_x and ν_y .

The distributions of the horizontal and vertical tunes at 18.3 kV and 20.4 kV EQS voltage in the $E_0 B_i$ configuration are illustrated by tune footprints in Fig. 6, where the vertical tunes of the particle distribution are plotted against their horizontal tunes as previously done in Ref. 17.

The tune footprints in Fig. 6 are shown together with resonance lines up to order 11. The closeness of the tunes, indicated by a circle in each of the distributions, to these resonance lines can explain stronger or weaker nonlinearities in the tune shifts and/or the normal form transformation, causing more spread-out tune footprints. According to Eq. 7, the normal form algorithm up to order m is only sensitive to resonances up to order $n = m + 1$, which is why resonances of order ten and 11 are indicated differently compared to resonances of order $n \leq 9$, since they only have an effect on the calculation of order 10.

The apparent difference between the tune footprint from the calculation with order eighth compared to the calculations with order ten are associated to the strong

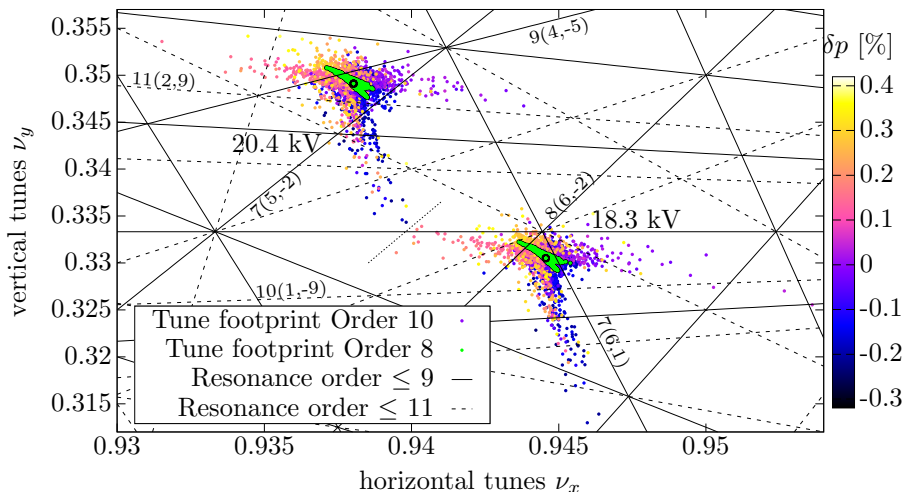


Fig. 6. The tune footprints at 18.3 kV and 20.4 kV EQS voltage. Resonance lines are denoted by $n(u, w)$. The tunes of the respective closed orbits are indicated by the circles. The difference between the eighth order and tenth order tune footprint calculation are significant due to strong nonlinearities of ninth order in the original maps. The short-dashed line in the middle shall clarify which particles belong to which distribution.

ninth order nonlinearities of the original map, since the additional resonance lines of tenth and 11th order are not closer to the reference tunes compared to the resonance lines of order $n \leq 9$.

The tune footprint for the different EQS voltages have a similar distribution for the order eight and order ten calculations, respectively. While the reference tunes are mainly determined by the EQS voltage, the relative tune shifts behave very similar. If the EQS voltage were to place the reference tunes very close to a resonance line, we expect the tune distribution and tune shifts to behave differently.

The distribution of the tenth order tune footprint has a T-shape. The positive horizontal tune shifts and negative vertical tune shifts are related to the generally positive horizontal and negative vertical tune shifts from phase space amplitudes and large momentum offsets. The negative horizontal tune shifts are combined effects with small positive momentum offsets $|\delta p| \leq 0.25\%$, which are negative in the horizontal component. It is likely that positive vertical tune shifts from small positive momentum offsets are canceled by the strong negative vertical tune shifts dependence on the horizontal phase space amplitude.

4.7. Comparison to preliminary tune measurements

A preliminary measurement¹⁸ using Fiber Harps in the muon $g-2$ storage ring investigated the tunes for the following EQS voltages: 13.0 kV, 15.0 kV, 17.6 kV, 19.0 kV, 20.2 kV and 20.5 kV. An interpolation of the data provides the following

relationship between the tunes ν_i and the EQS voltage V_{EQS}

$$\nu_x = 1.00155 \pm 0.00024 - V_{EQS}(0.00310 \pm 0.00001) \text{ and} \quad (10)$$

$$\nu_y = -0.0063 \pm 0.0022 + \sqrt{V_{EQS}}(0.0784 \pm 0.0006). \quad (11)$$

Evaluating the equations above for the two EQS voltages of our investigation yields

$$\begin{aligned} 18.3 \text{ kV: } \quad \nu_x &= 0.9448 \pm 0.0005 & \nu_y &= 0.3291 \pm 0.0048 \text{ and} \\ 20.4 \text{ kV: } \quad \nu_x &= 0.9383 \pm 0.0005 & \nu_y &= 0.3478 \pm 0.0049. \end{aligned} \quad (12)$$

The horizontal and vertical tunes ν_x and ν_y from our simulation are given in Table 1 are within the error margin of the interpolated measurement for both EQS voltages. The horizontal tunes from our simulation are generally smaller than the interpolated measurements, while the vertical tunes are generally larger. For both EQS voltages, the tunes of the most realistic simulation, namely E_0B_i , are always closest to the results from the interpolated measurement above. Large parts of the tune footprints in Fig. 6 are contained within the error margins of the respective measurement interpolation above. Thus, the preliminary tune measurement and our simulation show far reaching agreement.

5. Conclusion

DA normal form methods applied to Poincaré return maps of storage ring models provide a very versatile quantitative analysis of the tune shifts of the respective systems. Influences on the tune shifts can be associated to horizontal and vertical phase space amplitudes, changes in the system parameters, perturbations in the fields of components of the simulated storage ring, the closeness to resonances, the order of the calculation and nonlinearities in the original Poincaré return map.

For the example storage ring of the Muon $g-2$ Experiment, the results agree well with measurement results. In particular, the strong ninth order nonlinearities of the map caused by the 20th-pole of the EQS potential have a significant effect on amplitude and parameter dependent tune shifts. This manifests itself in the dominating eighth order dependencies in the amplitude and momentum dependent tune shifts and the drastic change in the tune footprint for calculations of order $m > 8$, which include the ninth order terms of the original map.

Future efforts focus on analyzing the more realistic E_fB_i case, for which the preparation of the transfer maps is still being studied, and investigating the related tune footprints in more detail, especially with regard to influences of nearby resonances.

Acknowledgments

This work was supported by the U.S. Department of Energy under Contract No. DE-SC0018636 and DE-AC02-07CH11359, and by the *Studienstiftung des deutschen Volkes* with a scholarship to one of the authors (A. W.). We thank A. Chapelain

for the data of the preliminary tune measurements with Fiber Harps, and we also thank K. Makino for various discussions and suggestions. Additionally, we greatly appreciate the insightful comments from the two reviewers of this paper.

References

1. M. Berz and K. Makino, *COSY INFINITY Version 10.0 Beam Physics Manual*, Tech. Rep. MSUHEP-151103-rev, Michigan State University (2017).
2. K. Makino and M. Berz, *Nuclear Instruments and Methods* **558**, 346 (2006), doi:10.1016/j.nima.2005.11.109.
3. J. P. Miller, E. De Rafael and B. L. Roberts, *Rept. Prog. Phys.* **70**, 795 (2007), doi:10.1088/0034-4885/70/5/R03, arXiv:hep-ph/0703049.
4. J. Grange, V. Guarino, P. Winter, K. Wood, H. Zhao, R. Carey, D. Gastler, E. Hazen, N. Kinnaird, J. Miller *et al.*, *arXiv:1501.06858* (2015).
5. D. Rubin, A. Chapelain, S. Charity, J. Crnkovic, F. Gray, W. Morse, J. Mott, J. Price, V. Tishchenko and W. Wu, Muon beam dynamics and spin dynamics in the g-2 storage ring, in *9th International Particle Accelerator Conference*, (2018), pp. 5029–5034.
6. M. Berz, *Modern Map Methods in Particle Beam Physics* (Academic Press, 1999).
7. M. Berz, *Nuclear Instruments and Methods A* **258**, 431 (1987), doi:10.1016/0168-9002(87)90927-2.
8. M. Berz, *Part. Accel.* **24**, 109 (1988).
9. J. F. Ritt and J. Liouville, *Integration in finite terms: Liouville's theory of elementary methods* (Columbia Univ. Press, 1948).
10. J. F. Ritt, *Differential equations from the algebraic standpoint* (American Mathematical Soc., Washington, D.C., 1932).
11. E. R. Kolchin, *Differential algebra & algebraic groups* (Academic press, 1973).
12. H. Poincaré, *Les méthodes nouvelles de la mécanique céleste* (Gauthier-Villars it fils, 1892, 1893, 1899).
13. J. Grote, M. Berz and K. Makino, *Nuclear Instruments and Methods A* **558**, 106 (2006), doi:10.1016/j.nima.2006.01.001.
14. D. Tarazona, M. Berz and K. Makino, Muon loss rates from betatron resonances at the Muon g-2 storage ring at Fermilab, in *10th Int. Charged Particle Optics Conf. (CPO-10)*, (Key West, USA, 2018). This volume.
15. Y. K. Semertzidis, G. Bennett, E. Efstathiadis, F. Krienen, R. Larsen, Y. Lee, W. M. Morse, Y. Orlov, C. S. Ozben, B. L. Roberts *et al.*, *Nuclear Instruments and Methods A* **503**, 458 (2003), doi:10.1016/S0168-9002(03)00999-9.
16. E. Valetovy, M. Berz and K. Makino, Computation of the main and fringe fields for the electrostatic quadrupoles of the Muon g-2 storage ring, in *10th Int. Charged Particle Optics Conf. (CPO-10)*, (Key West, USA, 2018). This volume.
17. K. Makino and M. Berz, *AIP CP* **530**, 217 (2000), doi:10.1063/1.1361680.
18. Preliminary data provided by the muon g-2 collaboration at fermilab.